Targeted dual-modality imaging of inflammation using 18 F-radiolabeled iron oxide microparticles

Amaury Guillou, Swannie Pedron, Nancy Alhaddad, Thomas Bonnard, Sara Martinez de Lizarrondo, Maxime Gauberti, Denis Vivien, Cécile Perrio

ACS APPLIED MATERIALS & INTERFACES

www.acsami.org

Research Article

Targeted Dual-Modality Imaging of Inflammation Using ^{18}F-Radiolabeled Iron Oxide Microparticles

Amaury Guillou,* Swannie Pedron,⊥ Nancy AlHaddad,⊥ Thomas Bonnard, Sara Martinez de Lizarrondo, Maxime Gauberti, Denis Vivien, and Cécile Perrio*

Cite This: *ACS Appl. Mater. Interfaces* 2025, 17, 63213−63222

Read Online

ACCESS | Metrics & More | Article Recommendations | Supporting Information

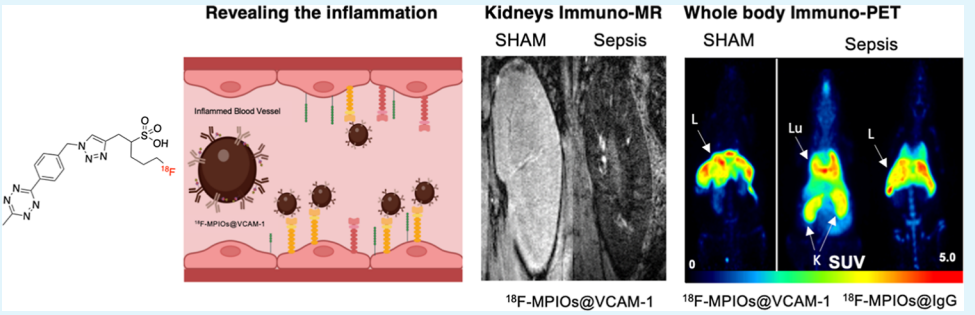

ABSTRACT: The ability to noninvasively map vascular inflammation with high spatial and molecular resolution remains a major challenge in biomedical imaging. The integration of both positron emission tomography (PET) and magnetic resonance imaging (MRI) through a dual-modality imaging probe represents a highly attractive approach. Here, we introduce a ^{18}F-labeled hydrophilic sulfotetrazine engineered for rapid and robust bioorthogonal inverse electron demand Diels−Alder (IEDDA) conjugation to BCN (bicyclo[6.1.0]nonyne)-functionalized microsized particles of iron oxides (MPIOs) targeting vascular cell adhesion molecules-1 (VCAM-1) known as key markers of endothelial inflammation. The clickable ^{18}F-reagent exhibits exceptional aqueous solubility and stability, fast second-order kinetics (k_2 = 827 $M^{-1}{\cdot}s^{-1}$) in the reaction with BCN, and compatibility with automated radiosynthesis platforms. We exploited this tool to generate dual-modality PET/MR ^{18}F-MPIOs@αVCAM-1 by conjugation with MPIOs coated with anti-VCAM-1 antibodies incorporating BCN. Dynamic immuno-PET/MR imaging in a murine model of LPS-induced sepsis revealed strong and specific tracer accumulation in lungs and kidneys in accordance with VCAM-1 overexpression, while high-resolution T2*-MRI confirmed cortical kidney retention with high precision. Thus, the ^{18}F-sulfotetrazine offers a powerful and modular strategy for late-stage functionalization of nanocarriers and sets the stage for the next generation of multimodal probes tailored for real-time tracking of inflammatory pathologies.

KEYWORDS: *inflammation, fluorine-18, MPIOs, ^{18}F-sulfotetrazine, click chemistry, immuno-PET-MR*

INTRODUCTION

Molecular imaging represents a pinnacle of diagnostic innovation, providing profound insights into cellular and molecular processes that underpin both physiological functions and pathological conditions.[1−3] This advanced imaging technology enhances our understanding of disease mechanisms, facilitating early diagnosis, monitoring, and treatment across a spectrum of medical disciplines. Of all current imaging techniques, positron emission tomography (PET) and magnetic resonance imaging (MRI) are distinguished by their complementary strengths, PET excels in identifying trace amounts of radiotracers with remarkable sensitivity, whereas MRI provides outstanding spatial resolution and rich soft-tissue contrast.[4−6] The convergence of PET and MRI thanks to bimodal PET-MR probes marks a significant evolution in medical imaging. These hybrid probes harness the molecular sensitivity of PET alongside the anatomical clarity of MRI, providing a composite image that delivers both functional and anatomical information.[7−9] Vascular inflammation represents a key feature of many acute and chronic diseases, including atherosclerosis, sepsis, and oncology. It is often characterized by endothelial activation and upregulation of cell adhesion molecules such as vascular cell adhesion molecule-1 (VCAM-1).[10−16] The noninvasive, real-time imaging of such endothelial markers holds enormous potential for early diagnosis and therapeutic monitoring. However, most

Received: September 11, 2025
Revised: October 23, 2025
Accepted: October 23, 2025
Published: November 10, 2025

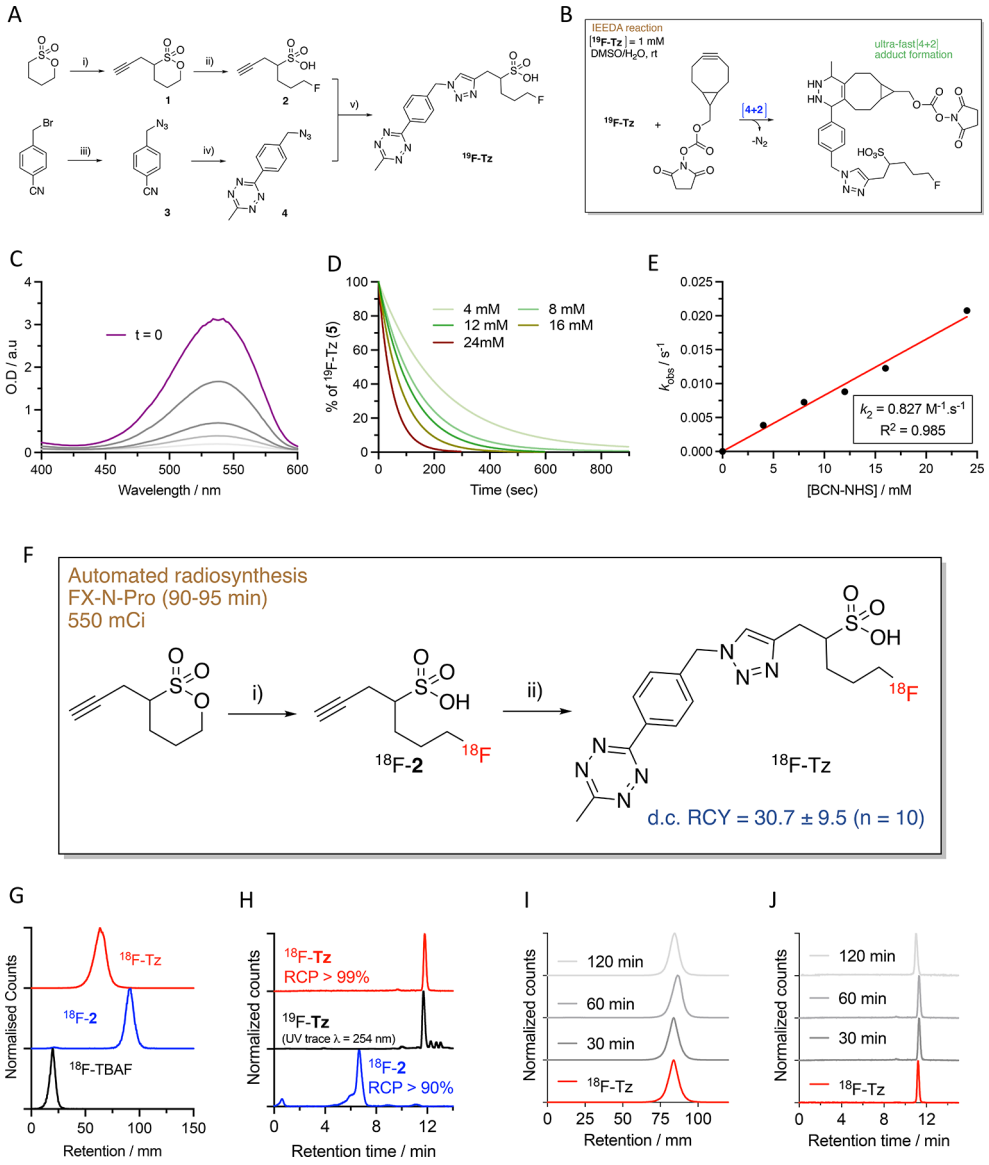

Figure 1. Synthesis, radiosynthesis, IEDDA kinetics, and in vitro stability. **A.** General synthesis scheme for the preparation of **1**. (i) *n*-BuLi, THF, −78 °C, 20 min then propargyl bromide, −78 °C, 1 h, 40%, (ii) CsF, K_{222}, CH_3CN, 120 °C, 25 min, 95%, (iii) NaN_3, KI, acetone, rt, 24 h, 99%, and (iv) 3-mercaptopropionic acid, $NH_2{\cdot}NH_2$, CH_3CN, EtOH, 45 °C, 24 h. $NaNO_2$, HCOOH, 0 °C, 2 h, 50% (v) **2** (1 equiv), **4** (1.2 equiv), $Cu(OAc)_2$ (0.1 equiv), Na-L-asc (0.1 equiv), acetone/H_2O (7:3), reflux, 2 h, 72%. **B.** General synthesis scheme for the IEDDA reaction between **1** and BCN−NHS. **C.** UV−visible spectra of **1** (1 equiv) over time upon addition of BCN−NHS (1 equiv) in solvent 1:10 DMSO/PBS 1X. **D.** Kinetic plots showing the change in the relative concentration of **5** (1 mM) vs time after the addition of different concentrations of BCN−NHS. **E.** Corresponding plot of the measured rate constants for the [4 + 2] cycloaddition of ^{19}F-Tz showing a linear relationship between BCN concentration and the click chemistry. **F.** General scheme for the automated radiosynthesis of ^{18}F-Tz. (i) **5** (5 mg), [^{18}F]fluoride, $TBAHCO_3$, CH_3CN, 105 °C, 15 min, 90−95%, (ii) Tz-N_3 (**2**), $Cu(OAc)_2$, Na-L-ascorbate, 60 °C, 25 min (for CuAAC coupling reaction) then $NaNO_2$, HCOOH, H_2O, 25 °C, 5 min (for oxidation step), 60−92%. **G.** Radio-iTLC (SiO_2, CH_3CN, H_2O 98/2, 0.1% TFA) characterization of ^{18}F-TBAF (black curve), ^{18}F-**2** (blue curve) and ^{18}F-**1** (red curve), showing full radiochemical conversion. **H.** Radio-HPLC characterization of ^{18}F-**2** (blue curve), **1** (black curve, UV trace), and ^{18}F-**1** (red curve), showing complete radiochemical purity (>98%). **I.** In vitro stability of ^{18}F-**1** in human serum up to 2 h post incubation monitored by radio-iTLC (SiO_2, CH_3CN, H_2O 98/2, 0.1% TFA). **J.** In vitro stability of ^{18}F-**1** in serum up to 2 h post incubation monitored radio-HPLC showing no degradation of the radiotracer.

current imaging modalities either lack the molecular specificity needed to detect early inflammatory changes or offer insufficient spatial resolution to resolve small vascular structure.

Molecular imaging using microparticles has emerged as a promising approach to overcome these limitations, enabling the development of contrast agents that can be both vectorizable and multimodal.[17] In particular, microparticles of iron oxide (MPIOs) provide high magnetic susceptibility, allowing sensitive detection by MRI, while their large surface area enables dense functionalization with targeting ligands or radionuclides.[10,18−21] The integration of MPIOs with PET could allow for quantitative and whole-body tracking of inflammation, but remains poorly exploited due to the challenge of stably incorporating a radioisotope. Most of the nanoparticles radiolabeling was performed using radiometals (^{68}Ga, ^{64}Cu, and ^{89}Zr) for their relatively easy and direct introduction by chelation.[22−26] However, despite its complex

https://doi.org/10.1021/acsami.5c18158
ACS Appl. Mater. Interfaces 2025, 17, 63213−63222

radiochemistry, fluorine-18 remains highly attractive due to its physical properties, convenient 109.7 min half-life, almost exclusive (97%) low-energy β+ decay (635 keV), and its highly efficient production by bombardment of protons on the $H_2[^{18}O]O$ target according to the $^{18}O(p, n)^{18}F$ nuclear reaction.[27−29] Despite the synthetic challenges of ^{18}F-labeling, recent strategies have enabled the efficient incorporation of fluorine-18 into nanoparticles under mild conditions.[30−32] Radiofluorinated reagents such as ^{18}F-SFB (N-succinimidyl-4-[^{18}F]fluorobenzoate) and ^{18}F-FBA (4-[^{18}F]fluorobenzoic acid) have been used to label amine-functionalized silica and lipid nanoparticles for in vivo PET imaging. "SiFA" approach allowed direct ^{18}F/fluoride exchange on silicon-containing surfaces.[33] These methods provided high radiochemical yields and preserved the nanoparticle integrity, supporting their clinical translation. Pioneering work by K. Barry Sharpless, Morten Meldal, and Carolyn Bertozzi, recognized with the 2022 Nobel Prize in chemistry, laid the foundation for bioorthogonal click chemistry, a class of highly selective reactions that can occur in biological environments without interfering with native biochemistry.[34] Among these, inverse electron-demand Diels−Alder (IEDDA) reactions between tetrazines and strained alkynes offer fast, selective, and aqueous-compatible conjugation strategies appropriate for PET probe development.[35] Yet, despite its promise, the application of IEDDA chemistry to create clinically relevant, multimodal nanoparticle systems has been limited by the availability of stable, hydrophilic, and high-yielding ^{18}F-labeled tetrazines.[36−38]

Here, we report the design and the synthesis of a ^{18}F-tetrazine optimized for aqueous solubility and stability, click reactivity, and radiochemical accessibility. We employed this ^{18}F-tetrazine to generate ^{18}F-labeled VCAM-1-targeted MPIOs via a one-step approach by an IEDDA reaction, yielding robust dual-modality immuno-PET-MR probes. In a mouse model of LPS-induced systemic inflammation, we demonstrated strong VCAM-1-dependent uptake in lungs and kidneys using hybrid PET-MR imaging, validated by high-resolution immuno-MRI. By merging PET's molecular sensitivity with MRI's detailed anatomical imaging, these innovative probes demonstrated to possess the potential to set new standards in the diagnosis and management of inflammatory diseases, embodying the cutting-edge of personalized medicine and offering a glimpse into the future of medical diagnostics.

RESULTS AND DISCUSSION

Synthesis, Radiosynthesis, and Reactivity toward BCN and In Vitro Stability of Tetrazine 1 and ^{18}F-1. The overall objective of the study was to develop and assess the ability of a new hydrophilic ^{18}F-fluorotetrazine to be used as a potential reagent for the later development of multimodal probes for dual immuno-PET-MR molecular imaging (Figure 1). Indeed, the water solubility of the ^{18}F-tetrazine was a key characteristic to perform conjugation to BCN-functionalized and antibody-coated MPIOs in a biocompatible buffer medium without any trace of organic solvent that would need to be removed before i.v. injection. We then exploited the new compound ^{18}F-1 bearing a SO_3^- (sulfo) group able to enhance hydrophilicity and to be directly generated by the original sultone ring opening reaction with cyclotron-produced [^{18}F]-fluoride.[39−41] The synthesis of nonradioactive reference tetrazine **1**, depicted in Figure 1A, was performed in a convergent manner using a modified published procedure. Full synthetic methodologies and characterization of tetrazine 1 can be found elsewhere.[40] Briefly, C-alkylation of 1,4-butane sultone with propargyl bromide after deprotonation with *n*-butyllithium at −78 °C, provided propargylic sultone **5** in 40% yield. Then, the nucleophilic-based sultone ring opening with CsF in the presence of $K_{2.2.2}$ yielded alkyne-modified fluorosulfonate **4** after tC_{18} purification in 95% yield. Azidotetrazine **2** was obtained from 4-bromomethylbenzonitrile in two steps by a substitution reaction with NaN_3 and then a Pinner reaction in 49.5% yield. Finally, by combining **2** and **4** using copper-catalyzed azide/alkyne "CuAAC" click reaction followed by oxidation, the desired fluorosulfotetrazine **1** was obtained in 86% yield after purification.

Bicyclo[6.1.0]nonyne (BCN) is often preferred over *trans*-cyclooctene (TCO) in bioorthogonal ligation due to its superior stability and ease of handling.[42] Although TCO exhibits faster kinetics in inverse electron-demand Diels−Alder (IEDDA) reactions, its tendency to isomerize and degrade under light or heat limits its practical use.[43] In contrast, BCN is chemically robust and synthetically accessible and offers sufficient reactivity for most biological applications. Its improved aqueous solubility and in vivo stability further enhance its utility in bioconjugation strategies. The ability of the novel clickable fluorosulfotetrazine 1 to be used in bioorthogonal reaction with strained alkyne was further studied by means of UV−visible measurements (Figure 1B−E). Tetrazine derivatives, which absorb in the range of 500−580 nm, served as useful chromophores for kinetic studies by tracking the UV transition's disappearance upon ligation with a BCN motif. As shown in Figure 1D, the time-dependent decrease of the tetrazine absorption at 520 nm upon the addition of BCN−NHS reflects the rapid consumption of the reactive tetrazine moiety. The pseudo-first-order rate constants derived from these decay curves were plotted against the BCN concentration (Figure 1E), yielding a linear relationship with a slope corresponding to a second-order rate constant of 827 M^{-1} s^{-1}, demonstrating a remarkably efficient rate under the conditions used. This rate surpasses many reported kinetic constants for other bioorthogonal reactions, including Staudinger ligation ($k = 10^{-3}$ $M^{-1}\cdot s^{-1}$),[44] CuAAC cycloadditions ($k = 10-60$ $M^{-1}\cdot s^{-1}$),[45] underscoring the effectiveness of the tetrazine-BCN combination ($k = 1-10^6$ $M^{-1}\cdot s^{-1}$).[46] The rapid reaction kinetics is particularly suited to match the half-life of fluorine-18, facilitating the use of this chemical ligation approach in developing ^{18}F-MPIOs@αVCAM-1 for targeted imaging.

The multistep radiosynthesis of ^{18}F-**1** was executed on a GE TRACERlab FX NPro module, as detailed in Figure 1F. Initially, [^{18}F]fluoride was trapped on a Sep-Pak Light QMA, and then eluted into the first reactor with a 0.1 M $TBAHCO_3$ solution in acetonitrile. The resulting ^{18}F-TBAF was dried by azeotropic distillation before the addition of propargylic sultone **5** in acetonitrile. The radiofluorination occurred at 105 °C for 15 min, and acetonitrile was then removed under reduced pressure. The propargylic ^{18}F-fluorosulfonate ^{18}F-**4** was purified by trapping unreacted ^{18}F-TBAF and the sultone precursor on a Sep-Pak Light QMA. Isolated ^{18}F-**4** was recovered in the second reactor by elution with acetone and then, after acetone elimination, mixed with sodium ascorbate and copper acetate in water. Azidotetrazine **2** in acetone was added, and the CuAAC reaction was conducted at 60 °C for 25 min. Following oxidation with sodium nitrite and formic acid in water at 25 °C for 5 min, the mixture was diluted, passed

https://doi.org/10.1021/acsami.5c18158
ACS Appl. Mater. Interfaces 2025, 17, 63213−63222

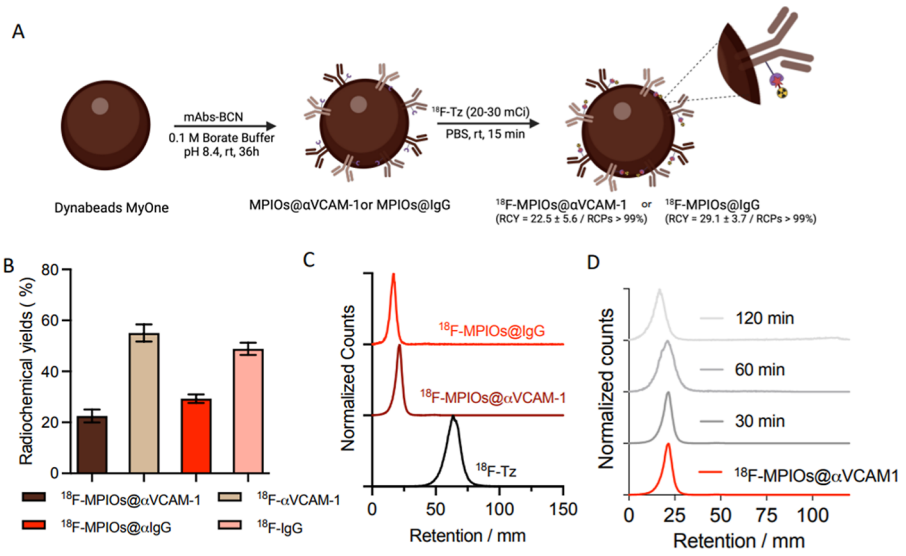

Figure 2. ^{18}F-radiolabeling of MPIOs using IEDDA approach. **A.** General synthesis scheme for the preparation of ^{18}F-MPIOs@αVCAM-1 and ^{18}F-MPIOs@IgG. **B**. Radiochemical yields for the radiosynthesis of ^{18}F-mAbs and ^{18}F-MPIOs@αVCAM-1 and ^{18}F-MPIOs@IgG (n = 5). **C**. Radio-iTLC characterization of ^{18}F-MPIOs@αVCAM-1 (brown curve) and ^{18}F-MPIOs@IgG (red curve). **D**. In vitro stability of ^{18}F-MPIOs@αVCAM-1 in serum up to 2 h post incubation monitored radio-iTLC (SiO_2, CH_3CN,H_2O 98/2, 0.1% TFA) showing no degradation of the bimodal probe.

through a Sep-Pak tC_{18} Plus Long Environmental cartridge, and the radioactive product was eluted with ethanol, then purified by semipreparative reverse-phase HPLC using phosphate buffer (pH 2.3)/EtOH 72:28 as eluent. After isolation and then addition of sodium bicarbonate in physiological serum, ^{18}F-**1** was obtained in PBS (pH 7.4) containing <10% EtOH, with an activity yield of 30.7 ± 9.5% (n = 10) after a total radiosynthesis time of 90−95 min and a specific activity of 137 GBq/μmol. Quality control using radio-iTLC and radio-HPLC confirmed the product's identity and purity and displayed >99% radiochemical purity (RCP). In vitro stability assays showed no degradation over 2 h after incubation of ^{18}F-**1** in human serum, confirming ^{18}F-**1** as a stable, clickable ^{18}F-labeled radiotracer. Hydrophilicity was confirmed by the negative mean LogP and LogD values of −1.3 and −1.7, respectively.[40]

IEDDA Reaction of ^{18}F-Tetrazine ^{18}F-1 with BCN-Antibodies. To enable site-accessible click conjugation, antibodies were first functionalized with strained cyclooctyne groups through lysine-selective coupling using a commercially available NHS−BCN ester. Based on literature, one can expect that this mild bioconjugation strategy resulted in efficient introduction of BCN handles (DOL = 1−3) on both a VCAM-1-specific monoclonal antibody and a nontargeting IgG control.[43,47] Subsequent strain-promoted IEDDA cycloaddition with ^{18}F-**1** carried out in PBS 1X buffer (pH 7.4) for 15 min at room temperature without adding organic solvent, afforded the corresponding radiolabeled conjugates ^{18}F-VCAM-1 and ^{18}F-IgG with radiochemical yields of 55.1 ± 7.5% and 48.9 ± 5.3%, respectively (n = 5, Figure 2B). These values, obtained for reactions under fully aqueous conditions, compare favorably to those of previously reported ^{18}F-antibody click-labeling strategies. For instance, Zhou et al. reported a 27−48% yield for ^{18}F-Tz click conjugation to anti-HER2 sdAb using ^{18}F-fluoronicotinyl precursor, while Zeglis et al. achieved 45 ± 5% for ^{18}F-DBCO-labeled huA33 via CuAAC chemistry.[48,49] The efficient, catalyst-free protocol presented here not only simplifies the workflow but also provides robust yields in aqueous medium-compatible antibody labeling.

Radiolabeling of MPIOs Using IEDDA Reaction and Stability Studies. Next we aimed at developing bimodal MPIOs targeting vascular endothelial cell adhesion molecules for immuno-PET-MR imaging (Figure 2). The constructs were designed based on microparticles of iron oxide (DynaBeads, Thermo Fisher) core on which BCN-modified antibodies (VCAM-1, or IgG isotype) were covalently introduced via nucleophilic substitution involving ε-lysine residue of the mAbs and the tosyl-activated microparticles shell. Some of us have previously reported that each MPIOs carries up to 10^9 antibodies.[50] With modified MPIOs in hand, radiolabeling experiments using the bio-orthogonal IEDDA approach were performed. For this, MPIOs@αVCAM-1 or MPIOs@IgG (corresponding to 2 × 10^9 beads) in PBS buffer (1X, pH 7.4) were incubated with ^{18}F-1 (370−720 MBq) in 4 mL of PBS (1X, pH 7.4) and mixed for 15 min. Then, magnetic purification of the crude reaction mixtures directly yielded ready-to-inject ^{18}F-MPIOs@αVCAM-1 or ^{18}F-MPIOs@IgG in 22.5 ± 5.6% and 29.1 ± 3.7% RCY (n = 5), respectively. The RCYs herein were lower than the one we obtained when only using BCN-modified mAbs (Figure 2B), which can be correlated with a lack of accessibility once grafted on the microparticle shell but are in the range of ^{18}F-radiolabeling of nanoprobes using click chemistry. Characterization of the radiolabeled MPIOs, as well as in vitro stability in a biological relevant set up, was performed by radio-iTLC analysis (Figure 2C,D). After incubation in human serum at 37 °C for up to 2 h, ^{18}F-MPIOs@αVCAM-1 was recovered totally unchanged, thus allowing their further in vivo evaluation as multimodal tracers.

Immuno-PET-MR Monitoring of LPS-Induced Inflammation. Lipopolysaccharide (LPS), a constituent of the outer membrane of Gram-negative bacteria, initiates an innate immune response by activating Toll-like receptor 4 (TLR4). The administration of LPS typically results in increased levels of VCAM-1 due to TLR4 activation and subsequent NF-κB signaling pathway activation. This upregulation aids the adhesion and migration of leukocytes to inflamed tissues, thereby amplifying the inflammatory response.[14,51,52] Given

https://doi.org/10.1021/acsami.5c18158
ACS Appl. Mater. Interfaces 2025, 17, 63213−63222

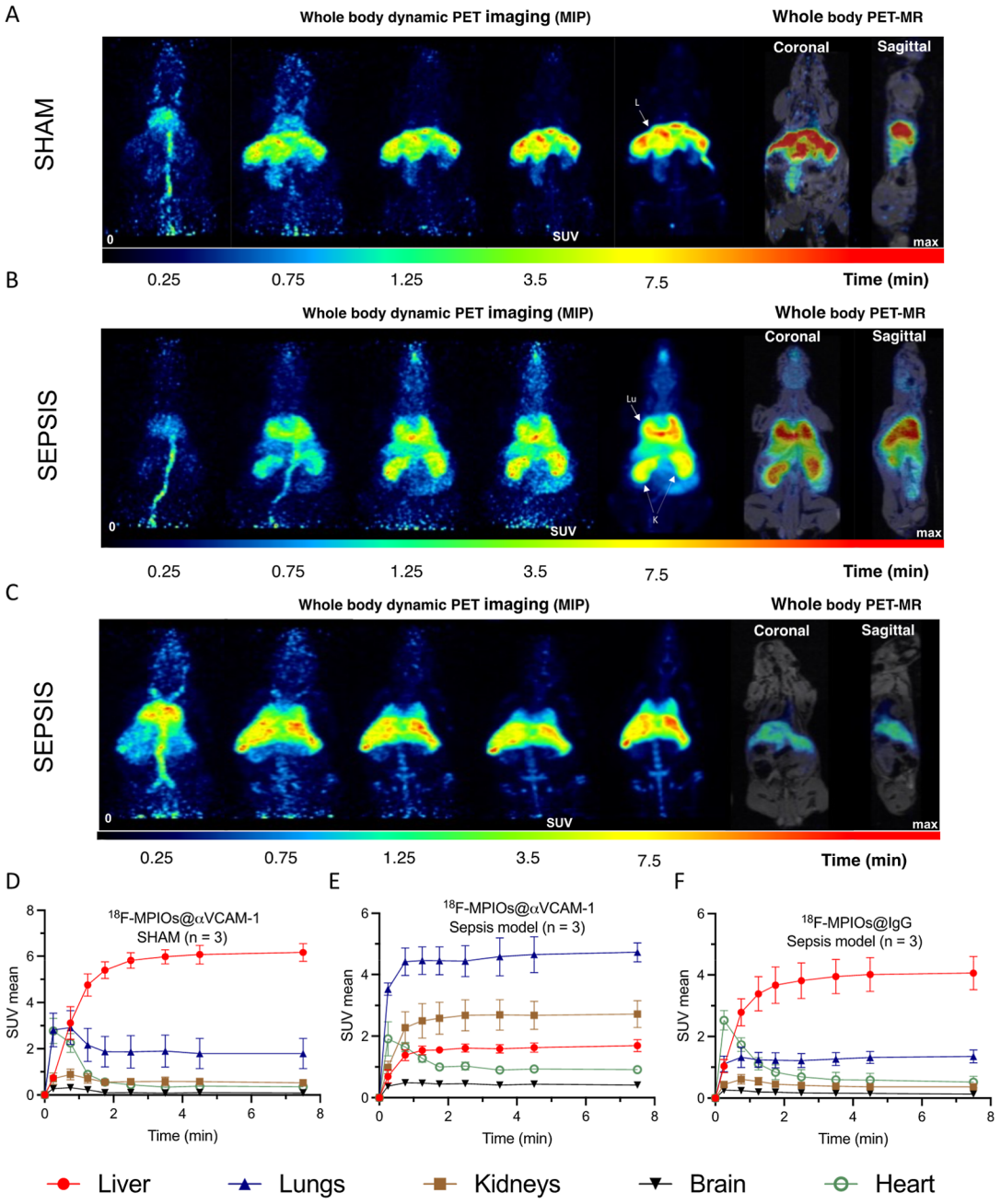

Figure 3. Hybrid immuno-PET MR dynamic images in healthy and sepsis model. **A.** Whole body dynamic PET-MR images of ^{18}F-MPIOs@αVCAM-1 in healthy animals. **B.** Whole body dynamic PET-MR images of ^{18}F-MPIOs@αVCAM-1 in an LPS-induced (5 mg/kg, i.p. injection) sepsis model. **C.** Whole body dynamic PET-MR images of ^{18}F-MPIOs@IgG in an LPS-induced (5 mg/kg, i.p. injection) sepsis model. **D.** Time activity curve of ^{18}F-MPIOs@αVCAM-1 in healthy mice (n = 3). **E.** Time activity curve of ^{18}F-MPIOs@αVCAM-1 in a LPS-induced (5 mg/kg, i.p. injection) sepsis model (n = 3). **F.** Time activity curve of ^{18}F-MPIOs@IgG in a LPS-induced (5 mg/kg, i.p. injection) sepsis model (n = 3).

that elevated VCAM-1 levels signify endothelial activation and inflammation, particularly in sepsis, targeting VCAM-1 with the developed molecular probes ^{18}F-MPIOs@αVCAM-1 could facilitate early diagnosis and monitoring of the disease. The imaging characteristics of the multimodal probe (^{18}F-MPIOs@αVCAM-1) were therefore assessed in vivo by using a combined PET/MRI (7T) system. This evaluation was conducted in a mouse model of sepsis, induced through an intraperitoneal injection of lipopolysaccharide (LPS, 5 mg/kg). In vivo dynamic PET imaging acquisitions were performed for up to 10 min postinjection to both healthy (SHAM, intraperitoneal injection of PBS) and LPS-induced sepsis models (Figure 3). Individual SUV_{mean} data derived from ROIs for ^{18}F-MPIOs@αVCAM-1 and ^{18}F-MPIOs@IgG are presented in Table S1. The pharmacokinetic profile and biodistribution of the particles across various organs (liver, kidneys, lungs, brain, heart, and muscle) were assessed in healthy and septic animals over a time frame of 10 min (Figures 3 and 4A). Standard uptake values (SUV_{mean}) were obtained by drawing ROIs from T1 3D MRI sequences for anatomical reference. While SHAM animals exhibited a biodistribution pattern dominated by hepatic uptake, with mean uptake progressively increasing from 0.25 min (SUV_{mean} = 0.74 ± 0.24, n = 3) to 5−10 min (SUV_{mean} = 6.16 ± 0.67, n

https://doi.org/10.1021/acsami.5c18158
ACS Appl. Mater. Interfaces 2025, 17, 63213−63222

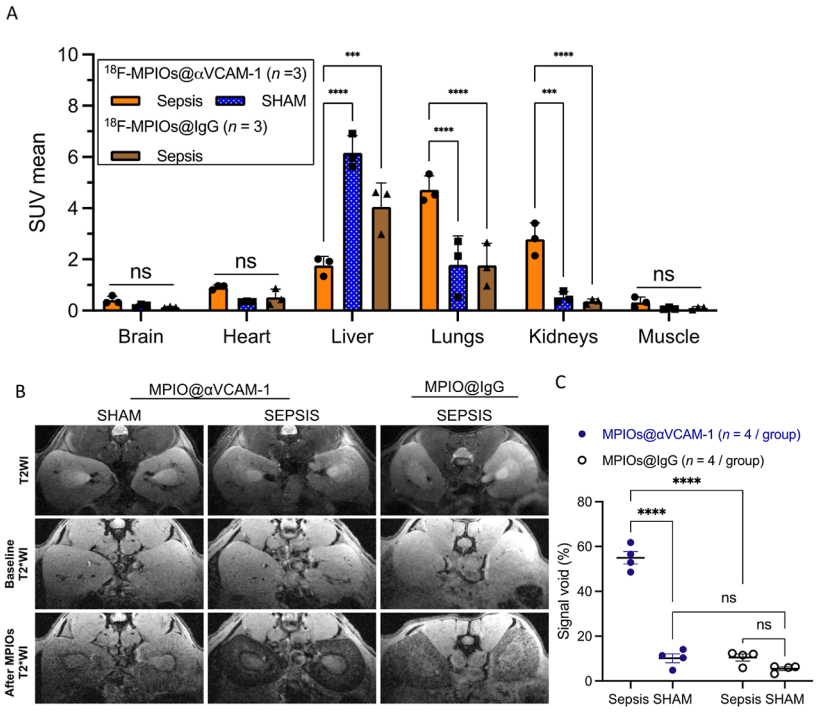

Figure 4. Hybrid immuno-PET MR in an LPS-induced sepsis model. **A.** Standard tracer uptake values quantification from in vivo PET acquisitions (n = 3, two-way ANOVA analysis with Bonferroni's multiple comparison test, *p < 0.05, **p < 0.01, ***p < 0.001, ****p < 0.0001). **B.** Kidney T2* MRI of a healthy and sepsis mouse before (baseline) and after injection of ^{18}F-MPIOs@αVCAM-1 or ^{18}F-MPIOs@IgG. **C.** Kidney immuno-MRI quantifications (signal void % of the percentage of hypo-intense voxels within the renal cortex relative to total cortical volume) reflecting MPIOs@αVCAM-1 or MPIOs@IgG accumulation (n = 4, two-way ANOVA analysis with Bonferroni's multiple comparison test, ****p < 0.0001).

= 3). This indicates a strong accumulation and possibly an active role in the metabolism or sequestration of these large particles via phagocytosis. The lungs exhibited an initial high uptake (SUV_{mean} = 2.81 ± 1.26 at 0.25 min, n = 3), which gradually decreased over time (SUV_{mean} = 1.79 ± 1.13 at 7 min, n = 3), suggesting initial accumulation followed by a wash-out of the microsized particles. Kidney concentrations decreased slightly, with the SUV_{mean} going from 0.70 ± 0.43 to 0.52 ± 0.21 (n = 3) in 10 min, while heart concentrations reduced more markedly, with the SUV_{mean} from 2.25 ± 0.70 to 0.35 ± 0.01. This biodistribution profile consisted of physiological nanoparticle clearance via Kupffer cells and the mononuclear phagocyte system.[53] This profile was notably altered in septic mice with a 3-fold decreased hepatic retention of ^{18}F-MPIOs@αVCAM-1 (SUV_{mean} = 1.69 ± 0.33, p < 0.0001 at 10 min, n = 3) observed in sepsis, suggesting that systemic inflammation reroutes circulating nanoparticles away from classical clearance organs toward inflamed vascular territories.

Further validation was provided by high-resolution immuno-MRI of the kidneys (Figure 4, B and C), which revealed a substantial percentage of hypo-intense voxels within the renal cortex relative to the total cortical volume (signal void %) in septic animals receiving nonradioactive analogs MPIOs@αVCAM-1 and MPIOs@IgG (50% loading), indicative of targeted MPIOs retention at sites of vascular inflammation. Quantitative MRI analysis (10 min postinjections) showed that the void volume fraction in the renal cortex reached 54.9 ± 5.59% in the sepsis group, compared to only 10.15 ± 3.0% in SHAM (p < 0.0001, n = 4) in LPS-treated animals injected with MPIOs@αVCAM-1. These hypo-intense regions corresponded anatomically to areas of dense peritubular capillary beds, which are known to express VCAM-1 during early sepsis.[54] Both PET and high resolution immuno-MRI revealed a consistent increase in renal signal following LPS treatment, with a 5.2-fold enhancement detected by PET (2.72 vs 0.52) and a 5.3-fold increase observed by MRI quantification (54.9 vs 10.4%) after injection of VCAM-1-targeted MPIOs, highlighting the complementarity of these two in vivo modalities for capturing inflammation-induced changes in kidney tracer accumulation. These findings not only validate VCAM-1 as a viable target for nanoparticle-based diagnostics in sepsis but also underscore the dynamic nature of nanoparticle biodistribution during systemic inflammation. The preferential accumulation in VCAM-1-rich tissues highlights the potential of this approach for real-time, noninvasive monitoring of vascular inflammation and for guiding targeted therapeutic delivery to sites of endothelial activation.

This difference in specific uptake is most evident in the lungs, where uptake of ^{18}F-MPIOs@αVCAM-1 increased a more than 2-fold in septic animals compared to SHAM controls (SUV_{mean} = 4.72 ± 0.54 vs 1.79 ± 1.12, n = 3, p < 0.0001) after 1 min postinjection and plateaued. This enhancement aligns with the well-documented overexpression of endothelial VCAM-1 in pulmonary vasculature in response to LPS-induced inflammation.[55] Given the lung's extensive capillary network and its early involvement in systemic inflammatory syndromes, the robust and statistically significant accumulation of targeted ^{18}F-MPIOs@αVCAM-1 supports its role as a primary site for VCAM-1-mediated molecular imaging. Similarly, kidneys demonstrated significantly elevated retention of targeted MPIOs in sepsis (SUV_{mean} = 2.72 ± 0.75 vs SUV_{mean} = 0.52 ± 0.22, n = 3, p < 0.01), likely reflecting upregulation of adhesion molecules in the glomerular and peritubular microvasculature, a phenomenon previously

https://doi.org/10.1021/acsami.5c18158
ACS Appl. Mater. Interfaces 2025, 17, 63213−63222

observed in both experimental and clinical models of endotoxemia.[56] Notably, nonspecific IgG-conjugated MPIOs (^{18}F-MPIOs@IgG) showed consistently low accumulation across all tissues and experimental groups (lungs: SUV_{mean} = 0.78 ± 0.16, $p < 0.0001$; kidneys: SUV_{mean} = 0.75 ± 0.15, $p < 0.001$, $n = 3$), confirming the high specificity of the VCAM-1 targeting strategy (Figures 3C and F, and 4).

CONCLUSIONS

In this study, we introduce the novel hydrophilic ^{18}F-fluorosulfotetrazine ^{18}F-**1** optimized for fast, chemoselective conjugation with BCN-modified microparticles of iron oxide (MPIOs). This platform enabled the rapid and stable radiolabeling of VCAM-1-targeted MPIOs under mild and aqueous conditions, resulting in highly pure, serum-stable bimodal probes compatible with PET and MRI. Using a murine model of systemic inflammation, we demonstrate that these ^{18}F-MPIOs@αVCAM-1 probes selectively accumulate in VCAM-1-rich organs such as the lungs and kidneys, revealing key sites of vascular inflammation through dynamic immuno-PET-MR imaging. These findings highlight the potential of bioorthogonal click chemistry to streamline the development of dual-modality imaging agents with high targeting specificity. Beyond their immediate utility in preclinical models, this strategy could lay the foundation for a new generation of modular, radiolabeled nanocarriers designed for real-time tracking of inflammation and the precision delivery of therapeutics. The use of 1 μm MPIOs in this study represents a deliberate preclinical design choice to maximize the MR contrast, magnetic susceptibility, and surface functionalization capacity, thereby enabling highly sensitive detection of endothelial targets. Although MPIOs are not suitable for systemic use in humans, the bioorthogonal labeling strategy and design principles demonstrated here are readily applicable to nanoparticle-based agents and offer a more clinically translatable platform. Future studies exploring the adaptation of this radiolabeling strategy to biocompatible nanoscale iron oxide platforms that exhibit favorable biodistribution, safety profiles, and regulatory precedent for clinical use are underway.

MATERIALS AND METHODS

[^{18}F]Fluoride was generated via the ^{18}O(p,n)^{18}F nuclear reaction by proton irradiation of ^{18}O-enriched water (97%, Eurisotop) using an IBA Cyclone 18/9 cyclotron. The automated radiosynthesis of ^{18}F-fluorosulfotetrazine (^{18}F-**1**) was carried out on a TRACERlab FX NPro module (GE Medical Systems).

Quality control and stability assessments were performed by using analytical HPLC on a Waters Alliance e2695 separation module equipped with a Waters 2998 photodiode array detector (190−380 nm) and a Berthold Herm LB 500 radioactivity detector. The analyses used a Gemini C_{18} column (5 μm, 4.6 × 250 mm, 110 Å) with a 0.7 mL/min flow rate and a linear gradient of solvent A (H_2O + 0.1% TFA) and solvent B (MeOH + 0.1% TFA), starting from 60% A (t = 0 min) to 5% A (t = 11 min). The UV/vis and radioactivity detectors were connected in series, with a temporal offset of approximately 0.10 to 0.30 min depending on temperature. Radiochemical identity was confirmed by coelution and retention time comparison with corresponding nonradioactive reference compounds via HPLC.

Radio-iTLC analyses were performed using CH_3CN/H_2O (98:2, v/v) containing 0.1% TFA as the mobile phase on silica-coated gel plates. The plates were analyzed using an Elysia-Raytest Rita Star 2018203 reader.

Radiosynthesis of ^{18}F-1. A cyclotron-produced [^{18}F]fluoride solution in ^{18}O-enriched water was trapped on a preconditioned Sep-Pak Light QMA cartridge and eluted with tetrabutylammonium bicarbonate (0.1 M, 200 μL) in acetonitrile (800 μL) to yield ^{18}F−TBAF (18−20 GBq). The eluate was dried under vacuum (65 °C for 6 min, then 95 °C for 3 min). After cooling to 70 °C, propargylic sultone 5 (5 mg in 1.6 mL of CH_3CN) was added and heated at 105 °C for 15 min to give crude ^{18}F-4, which was concentrated under reduced pressure. The residue was dissolved in acetone, passed through a Sep-Pak Light QMA cartridge, and combined with a second similar eluate. After mild evaporation, sodium ascorbate (30 mg, 150 μL H_2O) and copper(II) acetate (8.4 mg, 150 μL H_2O) were mixed and added under helium flow, followed by azidotetrazine 2 (5.1 mg in 350 μL acetone). The reaction was heated at 60 °C for 25 min and then treated with sodium nitrite (30 mg in 300 μL H_2O) and formic acid (100 μL) at 25−30 °C for 5 min. The mixture was diluted with water (2 × 5 mL), loaded onto a preconditioned Sep-Pak tC18 cartridge, washed (2 × 10 mL of H_2O), and eluted with ethanol (1.5 mL). The ethanolic fraction was diluted in phosphate buffer (3.5 mL, pH 2.3) and purified by semipreparative RP-HPLC. The product, ^{18}F-fluorosulfotetrazine (^{18}F-1), was collected in phosphate buffer/ethanol (72:28, v/v) and neutralized with sodium bicarbonate in saline. Using this automated process, ^{18}F-1 was obtained in 3.7−5.0 GBq (100−135 mCi) with a radiochemical yield of 30.7 ± 9.5% (n = 10) and a total synthesis time of approximately 90−95 min.

Preparation of BCN-Functionalized Monoclonal Antibodies. A 500 μL solution of VCAM-1 or IgG antibodies at 1 mg/mL (corresponding to approximately 0.5 mg, or 3.33 nmol, for a 150 kDa IgG) was adjusted to pH 8.3−8.5 using 0.1 M borate buffer. BCN−NHS ester (10 mM in anhydrous DMSO) was then added dropwise to a final 20-fold molar excess (6.7 μL; 66.7 nmol), with gentle mixing (final DMSO concentration ≈1.3% v/v). The reaction mixture was incubated for 4 h at room temperature. Following incubation, the conjugate was purified by spin-filtration using a 10 kDa Amicon Ultra device with three to four diafiltration cycles against PBS to remove unreacted reagent and DMSO. The purified BCN-modified antibody was finally reconstituted in 1000 μL of PBS for subsequent use.

MPIOs Synthesis and Radiolabeling. Dynabeads MyOne tosyl-activated (50 μL ≈ 5 × 10^8 beads/animal) were placed into a 15 mL Falcon tube and filled with 2.5 mL of borate buffer (1.0 M, pH 8.4). Then the particles were magnetically filtered, and the supernatant was removed. Borate buffer was added (2.5 mL), and the operation was performed twice again. Then, a solution of BCN-modified VCAM-1 or BCN-modified IgG control (0.5 mg/mL, 200 μL, or 100 μL for 50% loading) was added. To this solution was added 3 M ammonium sulfate (750 μL) and borate buffer (0.1 M, pH 8.4, 1300 μL). The particles were incubated for 36−48 h with shaking at 37 °C. The tube was placed on the magnet, and the supernatant was removed. 2.5 mL of blocking buffer (BSA, 5 g/L, Tween 20 10% v:v, PBS 1X pH 7.4) was added, and the particles were incubated for 24 h with shaking at 37 °C. Then, modified MPIOs were sonicated for 1 min. The supernatant was removed, and 2.5 mL of the particles was washed three times with PBS 1X containing BSA (1 g/L, Tween 20 10% v:v, PBS 1X pH 7.4). Finally, the supernatant was removed, and 4 mL of washing buffer was added, prior to sonication and storage of the modified MPIOs at 4 °C. ^{18}F-MPIOs@αVCAM-1 and ^{18}F-MPIOs@IgG were prepared by mixing ^{18}F-Tz (370−720 MBq) with 4 mL of MPIOs@αVCAM-1 or MPIOs@IgG (2 × 10^9 beads) for 15 min at room temperature. Caution! Radiolabeling experiments and magnetic purification were performed manually by experienced individuals and were performed in a shielded fume-hood to avoid unnecessary radiation exposure. ^{18}F-MPIOs@VCAM-1 and ^{18}F-MPIOs@IgG were resuspended in 4 mL (BSA, 5 g/L, Tween 20 10% v:v, PBS 1X pH 7.4) prior to in vivo administration.

In Vitro Human Serum Stability. For each experiment, ∼2 MBq of ^{18}F-**1** or ^{18}F-MPIOs@αVCAM-1 were mixed in 200 μL of human serum. The samples were incubated at 37 °C for 2 h. The dissociation of the radiolabeled particles was monitored by radio-iTLC (SiO_2, CH_3CN/H_2O 0.1%TFA 98/2). Experiments were performed in triplicate.

Animal Models. All animal procedures complied with the European Directive 2010/63/EU and national regulations and were conducted in authorized facilities (GIP Cyceron; E14118001)

https://doi.org/10.1021/acsami.5c18158
ACS Appl. Mater. Interfaces 2025, 17, 63213−63222

following approval by the regional ethics committee of Normandy (CENOMEXA, APAFIS#22318). Healthy male SWISS mice (8−10 weeks old) were obtained from the in-house breeding colony of the Centre Universitaire de Ressources Biologiques (CURB; A14118015). Animals were group-housed (≥2 per cage) under standard 12 h light/dark cycles with ad libitum access to food and water. Sepsis was induced by a single intraperitoneal injection of lipopolysaccharide (LPS; *E. coli* O111:B4, Sigma-Aldrich; 5 mg/kg). Immediately after, mice received buprenorphine (0.1 mg/kg, sc) to minimize pain or distress. Within 24 h, all LPS-treated mice displayed typical signs of sepsis, including piloerection, periorbital darkening, and reduced activity, with no interindividual variation observed. During all imaging and experimental procedures, animals were anesthetized with isoflurane (induction 5%, maintenance ∼2.5%, in 70% N_2O/30% O_2), and body temperature was maintained at 37.5 °C using a feedback-controlled heating system. A tail vein catheter (Insyte Autoguard, BD Medical, USA) was placed for intravenous administration.

PET-MR Experiments. Experiments were carried out on a small animal PET-MRI (7T) system (Bruker, Germany). In total, 3 mice groups were studied; healthy controls and sepsis models were injected with ^{18}F-MPIOs@αVCAM-1 and ^{18}F-MPIOs@IgG particles. Mice were anesthetized with isoflurane (1.5 to 2.0%) and maintained at 37 °C by the integrated heat animal holder, and the breathing rate was monitored during the imaging procedure. A catheter was inserted into the tail vein of mice for intravenous administration of the contrast agent. For anatomical MRI reference, T1_Fisp_3D scans were performed, including 3 stitched volumes, allowing us to obtain a whole body image of a mice, with the following parameters: 3D, repetition time (TR) 5.5 ms, echo time (TE) 2.6 ms, number of averages (NA) 3, voxel spacing 0.5/0.5/0.5 mm, and a field of view (FOV) 40/40/108 mm. High-resolution T2*-weighted images of kidneys for immuno-MRI were acquired with a surface coil (Bruker, Germany), using a 3D FLASH gradient echo imaging yielding an in-plane resolution of 78 × 156 μm^2 and a slice thickness of 300 μm (axial orientation) to ensure optimal sensitivity to MPIO-induced signal voids with TE/TR 8.6 ms/50 ms and a flip angle of 20°. One baseline scan was performed before the injection of the particles and one after the PET acquisition. List mode PET data were acquired for 10 min, and this was initiated as soon as the formulated ^{18}F-MPIOs@αVCAM-1 or ^{18}F-MPIOs@IgG were injected in order to monitor the bolus. The concentration of the probe was maintained between 1 and 4 mg [Fe]/kg and 1 to 15 MBq per animal. A second similar T2*-weighted image of kidneys was finally acquired to detect the magnetic particles accumulated 10 min after injection.

Images Analysis. PET data were normalized to correct for variations in system response, including attenuation, random coincidences, dead-time losses, positron branching ratio, and radioactive decay from the time of injection. List-mode data were acquired for 10 min, starting immediately after injection of ^{18}F-MPIOs@αVCAM-1 or ^{18}F-MPIOs@IgG. Dynamic images were reconstructed using an iterative MAP 0.5 algorithm and divided into eight frames (4 × 30, 3 × 60, and 1 × 300 s). Images were decay-corrected and normalized to the injected activity to express voxel values in %ID/cm^3 (equivalent to %ID/g assuming tissue density = 1). Quantitative analysis was performed with PMOD 3.7 software (PMOD Technologies, Zurich, Switzerland). Time−activity curves (TACs) were obtained by manually delineating 3D volumes of interest (VOIs) to calculate the mean and maximum radioactivity (% ID/cm^3), corrected to the injection time. Results were expressed as standardized uptake values (SUV_{mean}), defined as the ratio of tissue radioactivity concentration to injected dose normalized by body weight. For kidney MRI data, analyses were conducted in Image. Regions of interest were drawn over renal areas, and the signal void percentage was calculated by comparing pre- and post-injection scans.

Statistical Analysis. Results are presented as mean values ±SD. Statistical analysis was performed with GraphPad Prism software (v10.0). Where appropriate, data were analyzed by the unpaired, two-way ANOVA followed by Bonferroni's multiple comparison test.

■ ASSOCIATED CONTENT

Supporting Information

The Supporting Information is available free of charge at https://pubs.acs.org/doi/10.1021/acsami.5c18158.

Complete PET quantification data set including SUV_{mean} values for all animals (PDF).

■ AUTHOR INFORMATION

Corresponding Authors

Amaury Guillou − *Normandie Université, UNICAEN, CNRS, CEA, UAR3408, Cyceron Bd Henri Becquerel, 14000 Caen, France; Normandie Université, UNICAEN, INSERM, PhIND, Institut Blood and Brain @Caen-Normandie, 14000 Caen, France;* orcid.org/0000-0002-2455-9293; Email: guillou@cyceron.fr

Cécile Perrio − *Normandie Université, UNICAEN, CNRS, CEA, UAR3408, Cyceron Bd Henri Becquerel, 14000 Caen, France;* orcid.org/0000-0001-6559-3861; Email: perrio@cyceron.fr

Authors

Swannie Pedron − *Normandie Université, UNICAEN, INSERM, PhIND, Institut Blood and Brain @Caen-Normandie, 14000 Caen, France*

Nancy AlHaddad − *Normandie Université, UNICAEN, CNRS, CEA, UAR3408, Cyceron Bd Henri Becquerel, 14000 Caen, France*

Thomas Bonnard − *Normandie Université, UNICAEN, INSERM, PhIND, Institut Blood and Brain @Caen-Normandie, 14000 Caen, France;* orcid.org/0000-0003-0412-8223

Sara Martinez de Lizarrondo − *Normandie Université, UNICAEN, INSERM, PhIND, Institut Blood and Brain @Caen-Normandie, 14000 Caen, France*

Maxime Gauberti − *Normandie Université, UNICAEN, INSERM, PhIND, Institut Blood and Brain @Caen-Normandie, 14000 Caen, France; CHU Caen, Department of Diagnostic Imaging and Interventional Radiology, Caen 14000, France*

Denis Vivien − *Normandie Université, UNICAEN, INSERM, PhIND, Institut Blood and Brain @Caen-Normandie, 14000 Caen, France; CHU Caen, Clinical Research Department, Caen 14000, France*

Complete contact information is available at: https://pubs.acs.org/10.1021/acsami.5c18158

Author Contributions

⊥S.P. and N.H contributed equally to the work. The manuscript was written through the contributions of all authors.

Notes

The authors declare no competing financial interest.

■ ACKNOWLEDGMENTS

A.G. thanks the European Union's Horizon 2020 research and innovation programme under the Marie Skłodowska-Curie (grant agreement no. 101034329) and the Normandy Region under the WINNINGNormandy program for financial support. The authors thank the Normandy Region and France Life Imaging for further financial support. They also thank Hanadi Skeif and Vincent Mouton for the cyclotron supply of fluorine-18, Romaric Saulnier for tremendous help in animal

surgery, Mikaël Naveau for PET and MR sequence development and acquisition, and Stephane Guillouet for radiosynthesis automated assistance.

REFERENCES

(1) Ametamey, S. M.; Honer, M.; Schubiger, P. A. Molecular Imaging with PET. *Chem. Rev.* **2008**, *108* (5), 1501−1516.
(2) Dilsizian, V.; Chandrashekhar, Y. Molecular Imaging: New Promises. *JACC Cardiovasc Imaging* **2022**, *15* (11), 2019−2021.
(3) Zhang, K.; Xu, H.; Li, K. Molecular Imaging for Early-Stage Disease Diagnosis. *Adv. Exp. Med. Biol.* **2023**, *1199*, 39−58.
(4) Jennings, L. E.; Long, N. J. Two Is Better than One'—Probes for Dual-Modality Molecular Imaging. *Chem. Commun.* **2009**, *0* (24), 3511−3524.
(5) Louie, A. Multimodality Imaging Probes: Design and Challenges. *Chem. Rev.* **2010**, *110* (5), 3146−3195.
(6) Frullano, L.; Meade, T. J. Multimodal MRI Contrast Agents. *JBIC Journal of Biological Inorganic Chemistry* **2007**, *12* (7), 939−949.
(7) Ni, D.; Ehlerding, E. B.; Cai, W. Multimodality Imaging Agents with PET as the Fundamental Pillar. *Angew. Chem., Int. Ed. Engl.* **2019**, *58* (9), 2570−2579.
(8) Wei, X.; Zhao, H.; Huang, G.; Liu, J.; He, W.; Huang, Q. ESMION-Based Dual-Modality PET/MRI Probes for Acidic Tumor Microenvironment Imaging. *ACS Omega* **2022**, *7* (4), 3442−3451.
(9) Gholami, Y. H.; Yuan, H.; Wilks, M. Q.; Maschmeyer, R.; Normandin, M. D.; Josephson, L.; El Fakhri, G.; Kuncic, Z. A Radio-Nano-Platform for T1/T2 Dual-Mode PET-MR Imaging. *Int. J. Nanomedicine* **2020**, *15*, 1253−1266.
(10) Belliere, J.; Martinez de Lizarrondo, S.; Choudhury, R. P.; Quenault, A.; Le Béhot, A.; Delage, C.; Chauveau, D.; Schanstra, J. P.; Bascands, J.-L.; Vivien, D.; Gauberti, M. Unmasking Silent Endothelial Activation in the Cardiovascular System Using Molecular Magnetic Resonance Imaging. *Theranostics* **2015**, *5* (11), 1187−1202.
(11) Chen, Q.; Massagué, J. Molecular Pathways: VCAM-1 as a Potential Therapeutic Target in Metastasis. *Clin. Cancer Res.* **2012**, *18* (20), 5520−5525.
(12) Cheng, V. W. T.; de Pennington, N.; Zakaria, R.; Larkin, J. R.; Serres, S.; Sarkar, M.; Kirkman, M. A.; Bristow, C.; Croal, P.; Plaha, P.; Campo, L.; Chappell, M. A.; Lord, S.; Jenkinson, M. D.; Middleton, M. R.; Sibson, N. R. VCAM-1−Targeted MRI Improves Detection of the Tumor-Brain Interface. *Clin. Cancer Res.* **2022**, *28* (11), 2385−2396.
(13) Cheng, V. W. T.; Soto, M. S.; Khrapitchev, A. A.; Perez-Balderas, F.; Zakaria, R.; Jenkinson, M. D.; Middleton, M. R.; Sibson, N. R. VCAM-1-Targeted MRI Enables Detection of Brain Micrometastases from Different Primary Tumors. *Clin. Cancer Res.* **2019**, *25* (2), 533−543.
(14) Nachit, M.; Montemagno, C.; Clerc, R.; Ahmadi, M.; Briand, F.; Bacot, S.; Devoogdt, N.; Serdjebi, C.; Ghezzi, C.; Sulpice, T.; Broisat, A.; Leclercq, I. A.; Perret, P. Molecular Imaging of Liver Inflammation Using an Anti-VCAM-1 Nanobody. *Nat. Commun.* **2023**, *14* (1), 1062.
(15) Thayse, K.; Kindt, N.; Laurent, S.; Carlier, S. VCAM-1 Target in Non-Invasive Imaging for the Detection of Atherosclerotic Plaques. *Biology (Basel)* **2020**, *9* (11), 368.
(16) Nahrendorf, M.; Keliher, E.; Panizzi, P.; Zhang, H.; Hembrador, S.; Figueiredo, J.-L.; Aikawa, E.; Kelly, K.; Libby, P.; Weissleder, R. 18F-4V for PET-CT Imaging of VCAM-1 Expression in Inflammatory Atherosclerosis. *JACC Cardiovasc Imaging* **2009**, *2* (10), 1213−1222.
(17) Karageorgou, M.-A.; Bouziotis, P.; Stiliaris, E.; Stamopoulos, D. Radiolabeled Iron Oxide Nanoparticles as Dual Modality Contrast Agents in SPECT/MRI and PET/MRI. *Nanomaterials* **2023**, *13* (3), 503.
(18) McAteer, M. A.; von Zur Muhlen, C.; Anthony, D. C.; Sibson, N. R.; Choudhury, R. P. Magnetic Resonance Imaging of Brain Inflammation Using Microparticles of Iron Oxide. *Methods Mol. Biol.* **2011**, *680*, 103−115.
(19) Fournier, A. P.; Martinez de Lizarrondo, S.; Rateau, A.; Gerard-Brisou, A.; Waldner, M. J.; Neurath, M. F.; Vivien, D.; Docagne, F.; Gauberti, M. Ultrasensitive Molecular Imaging of Intestinal Mucosal Inflammation Using Leukocyte-Mimicking Particles Targeted to MAdCAM-1 in Mice. *Sci. Transl. Med.* **2020**, *12* (560), No. eaaz4047.
(20) Bonnard, T.; Gauberti, M.; Martinez de Lizarrondo, S.; Campos, F.; Vivien, D. Recent Advances in Nanomedicine for Ischemic and Hemorrhagic Stroke. *Stroke* **2019**, *50* (5), 1318−1324.
(21) Melemenidis, S.; Knight, J. C.; Kersemans, V.; Perez-Balderas, F.; Zarghami, N.; Soto, M. S.; Cornelissen, B.; Muschel, R. J.; Sibson, N. R. Vivo PET Detection of Lung Micrometastasis in Mice by Targeting Endothelial VCAM-1 Using a Dual-Contrast PET/MRI Probe. *Int. J. Mol. Sci.* **2024**, *25* (13), 7160.
(22) Burke, B. P.; Baghdadi, N.; Clemente, G. S.; Camus, N.; Guillou, A.; Kownacka, A. E.; Domarkas, J.; Halime, Z.; Tripier, R.; Archibald, S. J. Final Step Gallium-68 Radiolabelling of Silica-Coated Iron Oxide Nanorods as Potential PET/MR Multimodal Imaging Agents. *Faraday Discuss.* **2014**, *175* (0), 59−71.
(23) Boros, E.; Bowen, A. M.; Josephson, L.; Vasdev, N.; Holland, J. P. Chelate-Free Metal Ion Binding and Heat-Induced Radiolabeling of Iron Oxide Nanoparticles. *Chem. Sci.* **2015**, *6* (1), 225−236.
(24) Shi, S.; Xu, C.; Yang, K.; Goel, S.; Valdovinos, H. F.; Luo, H.; Ehlerding, E. B.; England, C. G.; Cheng, L.; Chen, F.; Nickles, R. J.; Liu, Z.; Cai, W. Chelator-Free Radiolabeling of Nanographene: Breaking the Stereotype of Chelation. *Angew. Chem., Int. Ed.* **2017**, *56* (11), 2889−2892.
(25) Patra, S.; Kancharlapalli, S.; Chakraborty, A.; Singh, K.; Kumar, C.; Guleria, A.; Rakshit, S.; Damle, A.; Chakravarty, R.; Chakraborty, S. Chelator-Free Radiolabeling with Theoretical Insights and Preclinical Evaluation of Citrate-Functionalized Hydroxyapatite Nanospheres for Potential Use as Radionanomedicine. *Ind. Eng. Chem. Res.* **2023**, *62* (7), 3194−3205.
(26) Shi, S.; Fliss, B. C.; Gu, Z.; Zhu, Y.; Hong, H.; Valdovinos, H. F.; Hernandez, R.; Goel, S.; Luo, H.; Chen, F.; Barnhart, T. E.; Nickles, R. J.; Xu, Z. P.; Cai, W. Chelator-Free Labeling of Layered Double Hydroxide Nanoparticles for in Vivo PET Imaging. *Sci. Rep.* **2015**, *5* (1), 16930.
(27) Lagunas-Solar, M. C.; Carvacho, O. F.; Cima, R. R. Cyclotron Production of PET Radionuclides: 18F (109.77 min; B+ 96.9%; EC 3.1%) from High-Energy Protons on Metallic Aluminum Targets. *Int. J. Radiation Applications and Instrumentation. Part A. Applied Radiation and Isotopes* **1988**, *39* (1), 41−47.
(28) Goud, N. S.; Joshi, R. K.; Bharath, R. D.; Kumar, P. Fluorine-18: A Radionuclide with Diverse Range of Radiochemistry and Synthesis Strategies for Target Based PET Diagnosis. *Eur. J. Med. Chem.* **2020**, *187*, 111979.
(29) Wang, Y.; Lin, Q.; Shi, H.; Cheng, D. Fluorine-18: Radiochemistry and Target-Specific PET Molecular Probes Design. *Front. Chem.* **2022**, *10*, 884517.
(30) Sun, Z.; Cheng, K.; Wu, F.; Liu, H.; Ma, X.; Su, X.; Liu, Y.; Xia, L.; Cheng, Z. Robust Surface Coating for a Fast, Facile Fluorine-18 Labeling of Iron Oxide Nanoparticles for PET/MR Dual-Modality Imaging. *Nanoscale* **2016**, *8* (47), 19644−19653.
(31) Teh, J. H.; Braga, M.; Allott, L.; Barnes, C.; Hernández-Gil, J.; Tang, M.-X.; Aboagye, E. O.; Long, N. J. A Kit-Based Aluminium-[18F]Fluoride Approach to Radiolabelled Microbubbles. *Chem. Commun. (Camb)* **2021**, *57* (88), 11677−11680.
(32) Deleuziere, M.; Benoist, E.-.; Quelven, I.; Gras, E.; Amiens, C. [18F]-Radiolabelled Nanoplatforms: A Critical Review of Their Intrinsic Characteristics, Radiolabelling Methods, and Purification Techniques. *Molecules* **2024**, *29* (7), 1537.
(33) Schirrmacher, E.; Wängler, B.; Cypryk, M.; Bradtmöller, G.; Schäfer, M.; Eisenhut, M.; Jurkschat, K.; Schirrmacher, R. Synthesis of P-(Di-Tert-Butyl[18F]Fluorosilyl)Benzaldehyde ([18F]SiFA-A) with High Specific Activity by Isotopic Exchange: A Convenient Labeling Synthon for the 18F-Labeling of N-Amino-Oxy Derivatized Peptides. *Bioconjugate Chem.* **2007**, *18* (6), 2085−2089.
(34) Nobel Prize in Chemistry Nature, 2022. https://www.nature.com/collections/ddgjcjgddi (accessed April 15, 2025).

https://doi.org/10.1021/acsami.5c18158
ACS Appl. Mater. Interfaces 2025, 17, 63213−63222

(35) Oliveira, B. L.; Guo, Z.; Bernardes, G. J. L. Inverse Electron Demand Diels–Alder Reactions in Chemical Biology. *Chem. Soc. Rev.* **2017**, *46* (16), 4895–4950.
(36) Andersen, I. V.; García-Vázquez, R.; Battisti, U. M.; Herth, M. M. Optimization of Direct Aromatic 18F-Labeling of Tetrazines. *Molecules* **2022**, *27* (13), 4022.
(37) Battisti, U. M.; Bratteby, K.; Jørgensen, J. T.; Hvass, L.; Shalgunov, V.; Mikula, H.; Kjær, A.; Herth, M. M. Development of the First Aliphatic 18F-Labeled Tetrazine Suitable for Pretargeted PET Imaging—Expanding the Bioorthogonal Tool Box. *J. Med. Chem.* **2021**, *64* (20), 15297–15312.
(38) Denk, C.; Svatunek, D.; Filip, T.; Wanek, T.; Lumpi, D.; Fröhlich, J.; Kuntner, C.; Mikula, H. Development of a 18F-Labeled Tetrazine with Favorable Pharmacokinetics for Bioorthogonal PET Imaging. *Angew. Chem., Int. Ed.* **2014**, *53* (36), 9655–9659.
(39) Schmitt, S.; Bouteiller, C.; Barré, L.; Perrio, C. Sultone Opening with [18F]Fluoride: An Efficient 18F-Labelling Strategy for PET Imaging. *Chem. Commun.* **2011**, *47* (41), 11465–11467.
(40) Beaufrez, J.; Guillouet, S.; Seimbille, Y.; Perrio, C. Synthesis, Fluorine-18 Radiolabeling, and In Vivo PET Imaging of a Hydrophilic Fluorosulfotetrazine. *Pharmaceuticals* **2023**, *16* (5), 636.
(41) Maingueneau, C.; Lafargue, A.-E.; Guillouet, S.; Fillesoye, F.; Cao Pham, T. T.; Jordan, B. F.; Perrio, C. 18F-Fluorination of Nitroimidazolyl-Containing Sultone: A Direct Access to a Highly Hydrophilic Radiotracer for High-Performance Positron Emission Tomography Imaging of Hypoxia. *JACS Au* **2024**, *4* (8), 3248–3257.
(42) Fawcett, C.; Watson, J.; Richards, S.; Doherty, A. E.; Seki, H.; Love, E. A.; Coles, C. H.; Coe, D. M.; Jamieson, C. Comparative Study of Click Handle Stability in Common Ligation Conditions. *Bioconjugate Chem.* **2025**, *36*, 1054.
(43) Béquignat, J.-B.; Ty, N.; Rondon, A.; Taiariol, L.; Degoul, F.; Canitrot, D.; Quintana, M.; Navarro-Teulon, I.; Miot-Noirault, E.; Boucheix, C.; Chezal, J.-M.; Moreau, E. Optimization of IEDDA Bioorthogonal System: Efficient Process to Improve Trans-Cyclooctene/Tetrazine Interaction. *Eur. J. Med. Chem.* **2020**, *203*, 112574.
(44) van Berkel, S. S.; van Eldijk, M. B.; van Hest, J. C. M. Staudinger Ligation as a Method for Bioconjugation. *Angew. Chem., Int. Ed.* **2011**, *50* (38), 8806–8827.
(45) Presolski, S. I.; Hong, V.; Cho, S.-H.; Finn, M. G. Tailored Ligand Acceleration of the Cu-Catalyzed Azide–Alkyne Cycloaddition Reaction: Practical and Mechanistic Implications. *J. Am. Chem. Soc.* **2010**, *132* (41), 14570–14576.
(46) Darko, A.; Wallace, S.; Dmitrenko, O.; Machovina, M. M.; Mehl, R. A.; Chin, J. W.; Fox, J. M. Conformationally Strained Trans-Cyclooctene with Improved Stability and Excellent Reactivity in Tetrazine Ligation. *Chem. Sci.* **2014**, *5* (10), 3770–3776.
(47) Baalmann, M.; Neises, L.; Bitsch, S.; Schneider, H.; Deweid, L.; Werther, P.; Ilkenhans, N.; Wolfring, M.; Ziegler, M. J.; Wilhelm, J.; Kolmar, H.; Wombacher, R. A. Bioorthogonal Click Chemistry Toolbox for Targeted Synthesis of Branched and Well-Defined Protein–Protein Conjugates. *Angew. Chem., Int. Ed.* **2020**, *59* (31), 12885–12893.
(48) Zhou, Z.; Devoogdt, N.; Zalutsky, M. R.; Vaidyanathan, G. An Efficient Method for Labeling Single Domain Antibody Fragments with 18F Using Tetrazine-Trans-Cyclooctene Ligation and a Renal Brush Border Enzyme-Cleavable Linker. *Bioconjugate Chem.* **2018**, *29* (12), 4090–4103.
(49) Zeglis, B. M.; Sevak, K. K.; Reiner, T.; Mohindra, P.; Carlin, S. D.; Zanzonico, P.; Weissleder, R.; Lewis, J. S. A Pretargeted PET Imaging Strategy Based on Bioorthogonal Diels-Alder Click Chemistry. *J. Nucl. Med.* **2013**, *54* (8), 1389–1396.
(50) Gauberti, M.; Montagne, A.; Quenault, A.; Vivien, D. Molecular Magnetic Resonance Imaging of Brain–Immune Interactions. *Front. Cell. Neurosci.* **2014**, *8*, 389.
(51) Kong, D.-H.; Kim, Y. K.; Kim, M. R.; Jang, J. H.; Lee, S. Emerging Roles of Vascular Cell Adhesion Molecule-1 (VCAM-1) in Immunological Disorders and Cancer. *Int. J. Mol. Sci.* **2018**, *19* (4), 1057.
(52) Martinez de Lizarrondo, S.; Jacqmarcq, C.; Naveau, M.; Navarro-Oviedo, M.; Pedron, S.; Adam, A.; Freis, B.; Allouche, S.; Goux, D.; Razafindrakoto, S.; Gazeau, F.; Mertz, D.; Vivien, D.; Bonnard, T.; Gauberti, M. Tracking the Immune Response by MRI Using Biodegradable and Ultrasensitive Microprobes. *Sci. Adv.* **2022**, *8* (28), No. eabm3596.
(53) Zelepukin, I. V.; Shevchenko, K. G.; Deyev, S. M. Rediscovery of Mononuclear Phagocyte System Blockade for Nanoparticle Drug Delivery. *Nat. Commun.* **2024**, *15* (1), 4366.
(54) Akhtar, A. M.; Schneider, J. E.; Chapman, S. J.; Jefferson, A.; Digby, J. E.; Mankia, K.; Chen, Y.; McAteer, M. A.; Wood, K. J.; Choudhury, R. P. In Vivo Quantification of Vcam-1 Expression in Renal Ischemia Reperfusion Injury Using Non-Invasive Magnetic Resonance Molecular Imaging. *PLoS One* **2010**, *5* (9), No. e12800.
(55) Meng, F.; Mambetsariev, I.; Tian, Y.; Beckham, Y.; Meliton, A.; Leff, A.; Gardel, M. L.; Allen, M. J.; Birukov, K. G.; Birukova, A. A. Attenuation of Lipopolysaccharide-Induced Lung Vascular Stiffening by Lipoxin Reduces Lung Inflammation. *Am. J. Respir. Cell Mol. Biol.* **2015**, *52* (2), 152–161.
(56) Oates, J. C.; Russell, D. L.; Van Beusecum, J. P. Endothelial Cells: Potential Novel Regulators of Renal Inflammation. *Am. J. Physiol Renal Physiol* **2022**, *322* (3), F309–F321.

https://doi.org/10.1021/acsami.5c18158
ACS Appl. Mater. Interfaces 2025, 17, 63213–63222